THE ASTROPHYSICAL JOURNAL, 384:482–490, 1992 January 10

X-RAY SPECTRAL VARIABILITY OF THE SEYFERT I GALAXY NGC 4051

HIDEYO KUNIEDA, SATIO HAYAKAWA, AND YUZURU TAWARA
Department of Astrophysics, Nagoya University, Furo-cho, Chikusa, Nagoya, Japan
KATSUJI KOYAMA
Department of Physics, Kyoto University, Kitashirakawa-oiwake-cho, Sakyo-ku, Kyoto, Japan
AND
SACHIKO TSURUTA AND KAREN LEIGHLY
Department of Physics, Montana State University, Bozeman, MT 59717
Received 1991 February 21; accepted 1991 July 19

ABSTRACT

The Seyfert I galaxy NGC 4051 was observed with the Japanese X-ray astronomy satellite *Ginga* in 1988 May. Fast variability of a factor of 2–3 within 1000 s is confirmed in the soft X-ray band (2.3–6.4 keV), and that of smaller amplitude within a few thousand seconds in the hard X-ray band (8.7–20.9 keV). A single power-law model cannot explain all the observed energy spectra. A blob ($N_{\rm blob} = 10^{24.5}$ cm^{-2}) model with intrinsically almost constant photon index of $\Gamma = 1.9$–2.0 is successfully applied to all the spectra. Intensity and spectral changes are well described by changes of intrinsic luminosity and the blob number ν in the line of sight. The observed variability time scale of $\sim$2000 s implies an upper limit of the central mass of $2 \times 10^7\ M_\odot$.

Subject headings: galaxies: individual (NGC 4051) — galaxies: Seyfert — X-rays: galaxies

1. INTRODUCTION

Active galactic nuclei (AGNs) emit strong radiation in a very wide energy range from radio to X-rays. If the components of radiation in different energy bands were emitted from the same spatial region by some related mechanisms, such as those assumed for the synchrotron–self-Compton model, the temporal variability of intensities in different bands would have to be correlated with each other. Simultaneous multifrequency observations of the Seyfert I galaxy NGC 4051 performed in 1988 May found a steady optical flux within 1%, while the X-ray flux varied by a factor of 2–3 on time scales of tens of minutes, thus ruling out the cospatial origin of IR/optical and X-rays (Done et al. 1990).

NGC 4051 is one of the nearest Seyfert I galaxies ($z = 0.0023$) and is suitable for the investigation of X-ray emission from AGNs because of the rather strong flux and fast variability. Marshall et al. (1983) found a doubling time scale of 2000 s with the imaging proportional counter (IPC) on board the *Einstein* satellite. A wide-band X-ray observation (0.05–10 keV) was performed by Lawrence et al. (1985) with a soft X-ray imaging telescope (LE) and large area detectors (ME) on board *EXOSAT*. Though variability faster than 1000 s was found, these authors pointed out that the amplitude of variability was dominated by variations on time scales of the order 1 hr. Matsuoka et al. (1990) found fast variability on a time scale of 2000 s in the first *Ginga* observation of NGC 4051 in 1987 with the large area counters (LAC). NGC 4051 is known as the second fastest variable Seyfert I galaxy after NGC 6814 (Tennant et al. 1981; Kunieda et al. 1990).

The X-ray spectrum was found to be softer when the source became brighter in both the *EXOSAT* observation (Lawrence et al. 1987) and the *Ginga* observation (Matsuoka et al. 1990). Hardening during the decrease of flux was described in terms of a decrease of the spectral slope, namely the power-law index.

In the second *Ginga* observation performed in 1988 May as a part of a simultaneous multi–wave band campaign organized by Tsuruta, significant X-ray temporal and spectral variabilities were observed. Comparing the intensities in the energy range above (H) and below (L) the iron K line, we found that in some cases the L-band flux varied nearly by a factor of 2, while the H-band flux stayed almost at a constant level, and that in some other cases both fluxes varied essentially together. In the latter synchronous cases and in the L-band flare, the spectra were approximately represented by a single power law. On the other hand, when the L-band flux was low but the H-band flux was high, the spectra were poorly fitted with a single power-law model. In the present paper, we present these X-ray results in greater detail and discuss one of the most promising models, a blob model, in which blobs are mainly responsible for the modulation of the soft X-ray spectrum, while the intrinsic emission spectrum does not radically change.

2. OBSERVATION

The *Ginga* detector (LAC) employed consists of eight multicell proportional counters with the total effective area of 4000 cm^2, covering the 2–20 keV band (Makino et al. 1987; Turner et al. 1989). The observation was performed in the MPC-1 mode, in which the signals from each layer of each detector were resolved into 48 pulse height channels with a time resolution of 16 s. In order to attain good statistics, we present count rates of the sum of the top and mid layers, per 256 s, in two energy bands (L, 2.3–6.4 keV; H, 8.7–20.9 keV).

NGC 4051 ($\alpha = 12^{\rm h}00^{\rm m}37^{\rm s}$, $\delta = 44°48'.7$: 1950) was observed from 1988 May 13.91 to 16.56 (UT) with the large area counters (LAC) on board *Ginga*. The total observation period is divided into 3 days, in each of which the X-ray flux level was $\sim$1 mCrab and the total observation time was on the order of 10^4 s (Table 1). The continual observations of 1000–2000 s were obtained with interruptions due to radiation belts and Earth occultations, as shown in the light curves in Figure 1.

Before and after the observation of NGC 4051, the detector axis pointed ($\alpha = 21^{\rm h}46^{\rm m}$, $\delta = 28°45'$) and ($\alpha = 11^{\rm h}46^{\rm m}$,

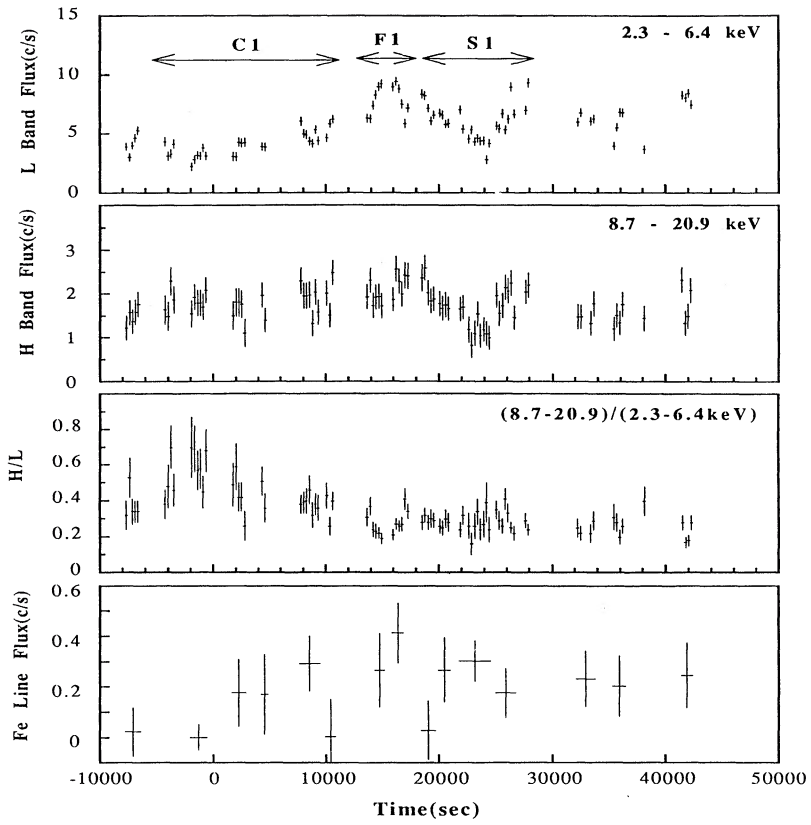

FIG. 1*a*

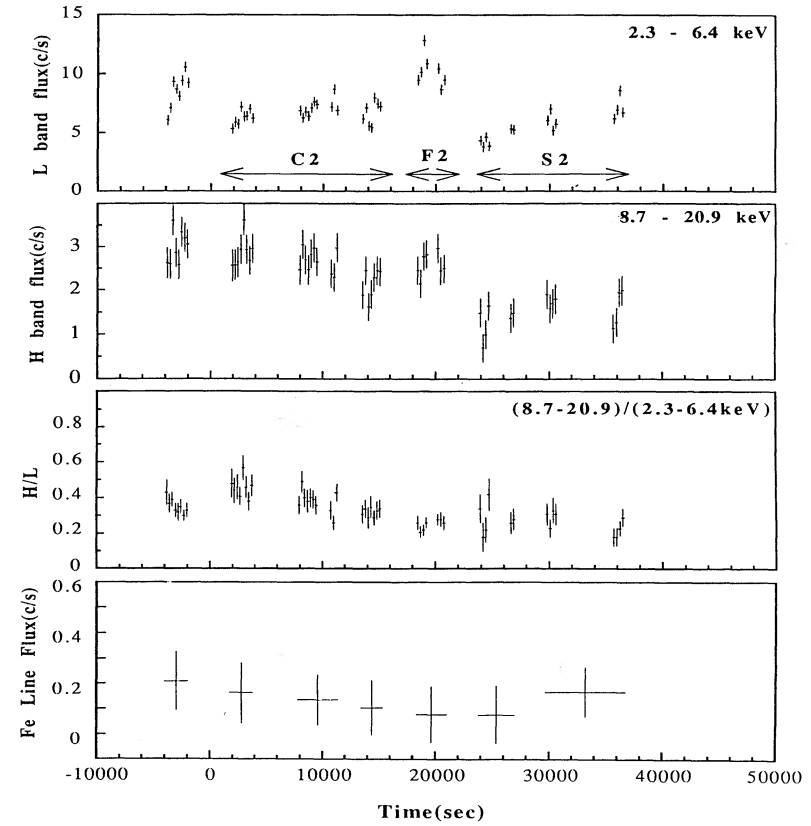

FIG. 1*b*

FIG. 1.—X-ray light curves of NGC 4051. X-ray light curves obtained by the top and mid layers in the *L* band (2.3–6.4 keV), the *H* band (8.7–20.9 keV), and the hardness ratio [(8.7–20.9)/(2.3–6.4)] are shown in (*a*) on May 14, in (*b*) on May 15, and in (*c*) on May 16. The light curve of iron line flux is also presented in the lowest panel of each figure.

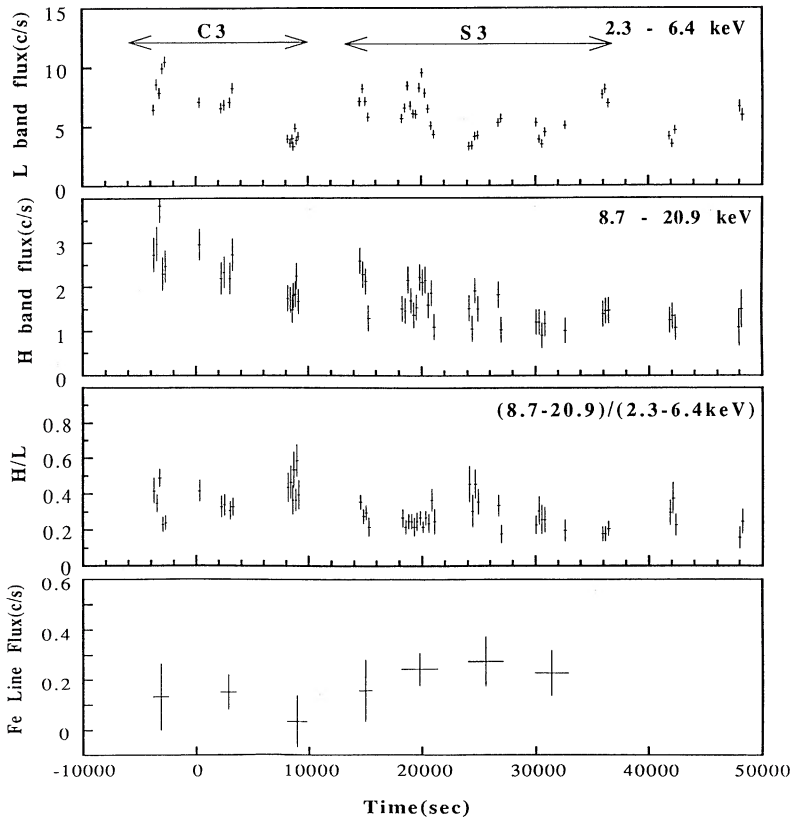

FIG. 1*c*

$\delta = 51°26'$), respectively, to obtain off-source background data. These data were almost identical and are combined to produce the off-source data base. The background counts result from the diffuse X-ray sky background, whose count rate is independent of the orbit phase, and from particles such as cosmic rays and precipitating electrons as well as their induced radioactivities. The count rate of the latter component depends on the geophysical environment and is positively correlated with the particle monitor rate. The source count rate is therefore obtained by subtraction of the off-source data from the on-source data at the same monitor level. Data with high monitor levels are discarded, since the subtraction procedure gives large errors. The reliability of this procedure is confirmed in two ways. First, a zero signal is observed above 25 keV after subtraction, at which the counter efficiency for X-rays is negligible. Second, the ratio of the count rate observed at the top and the mid layers is consistent with the ratio of their detection efficiencies expected for X-rays at all energies.

TABLE 1

OBSERVATION OF NGC 4051 WITH *Ginga* IN 1988

Day	Date (UT) (1988 May)	Exposure Time (s)	Average Flux (ergs cm^{-2} s^{-1})[a]
First	13(21:49)–14(11:45)	23552	2.1×10^{-11}
Second	14(22:53)–15(10:11)	14848	2.7×10^{-11}
Third	15(22:55)–16(13:26)	15616	2.2×10^{-11}

[a] (2–20 keV).

3. INTENSITY VARIATION

3.1. *Light Curves*

The light curves observed by the top and mid layers are presented for the *L* band (2.3–6.4 keV), *H* band (8.7–20.9 keV), and the hardness ratio (*H*/*L*). The lower energy limit of the *L* band is chosen to avoid the contribution of the soft excess component below 2 keV, which has been observed in many Seyfert galaxies (e.g., NGC 4051 by Lawrence et al. 1985, 3C 382 by Singh et al. 1990, and for others by Turner & Pounds 1990). The high-energy limit of the *H* band is chosen to discard the energy range with relatively high background level. The boundary of the two energy bands in the previous paper (Fig. 5 of Done et al. 1990) was selected to be at 8.7 keV. In order to separate two energy bands more clearly, we define the *L* band as the 2.3–6.4 keV interval and the *H* band as 8.7–20.9 keV with a gap of 6.4–8.7 keV where the iron K-line and the iron K-edge structure would appear.

The *L*- and *H*-band count rates after aspect correction are shown separately for three days in Figures 1*a*–1*c* together with the hardness ratio *H*/*L*. The abscissa represents time in seconds with 0 corresponding to 00:00 (UT) on May 14, 15, and 16, respectively. Each point gives the count rate averaged over 256 s with the vertical bar representing the 1 σ statistical error.

In the same figure, we compare the time variation of the iron K-line intensity which is derived by fitting the continuum spectrum with a single power law. Several points of 256 s accumulation within the time interval shown by a horizontal bar are combined in order to increase statistics for the iron line inten-

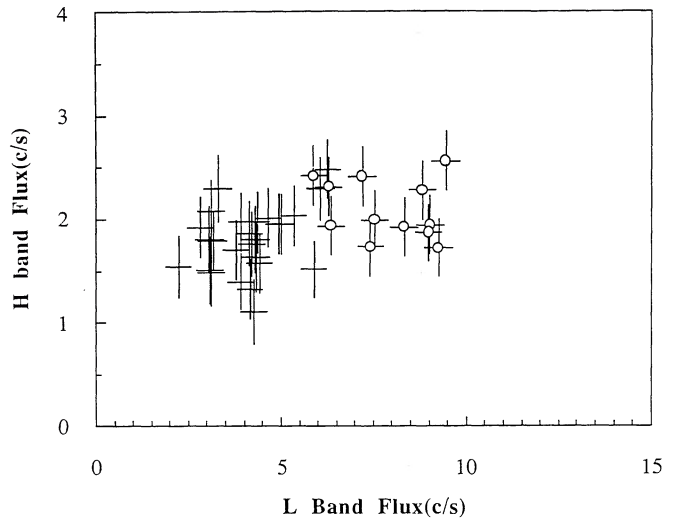

FIG. 2*a*

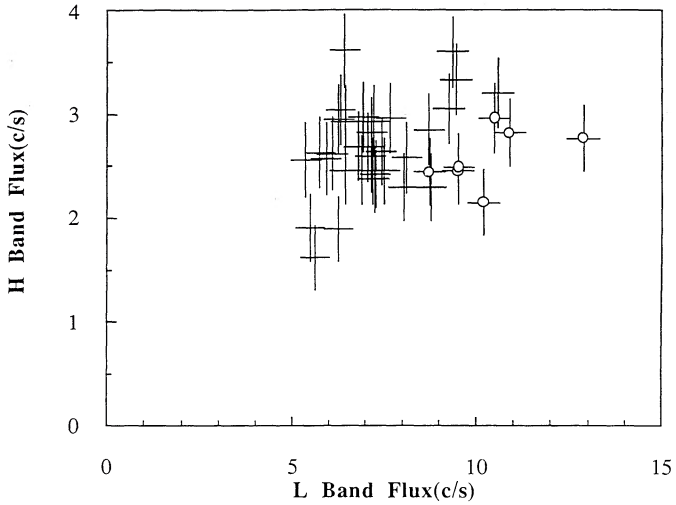

FIG. 2*b*

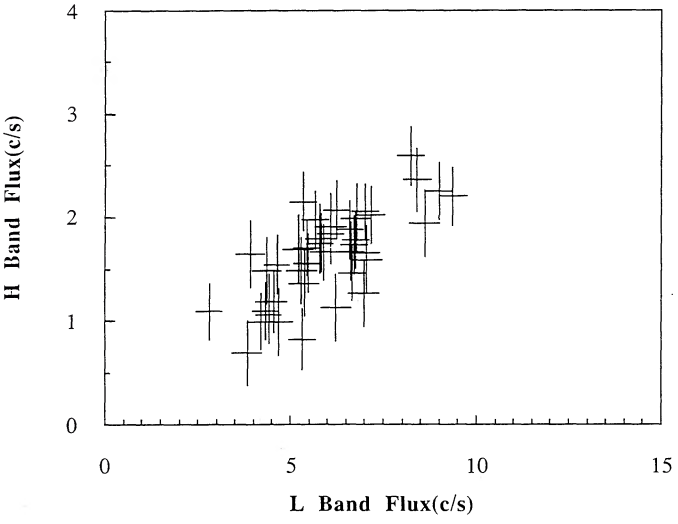

FIG. 2*c*

FIG. 2.—Correlation plots of the *L* and *H* band flux. The abscissa is the *L* band (2.3–6.4 keV) flux, and the ordinate is the *H* band (8.7–20.9 keV) flux. Fig. 2*a* shows the correlation plot in the C1 (*crosses*) and F1 (*open circles*) phases. Fig. 2*b* is the same plot in C2 (*crosses*) and F2 (*open circles*) phases. Fig. 2*c* shows that in the S phases.

sity. The average intensity in three days is 0.17 counts s^{-1} with a standard deviation of 0.10, which is comparable to the statistical error of each data point. Hence the time variability of the iron K-line intensity can hardly be claimed.

Looking at the light curves in Figure 1, one can readily notice features which indicate that the *H*-band flux is nearly constant during the early halves of the first and second days, while the *L*-band flux varies considerably. In the latter halves of these days and in most parts of the third day, on the other hand, both the *L*-band and *H*-band fluxes vary together. During the period with a constant *H*-band flux, the hardness ratio changes from a high value to a low value, the latter occurring when the *L*-band flux flares up at 15,000 s on the first day and at 20,000 s on the second day. Accordingly, we define three features, C, F, and S, which are characterized, respectively, by a constant *H*-band flux with a hard spectrum ($H/L > 0.3$), by a low energy (*L*-band) flare with a soft spectrum ($H/L < 0.3$), and by a soft spectrum of constant slope with variable flux (synchronized). These features on the first day are indicated as C1, F1, and S1 in Figure 1*a*. Similar features are seen also on the second day as shown with C2, F2, and S2 in Figure 1*b*. Such features, however, are not too conspicuous on the third day. On the third day, the *L*- and *H*-band fluxes are correlated, but the hardness ratio is high ($H/L > 0.3$) in the early part, and later it decreases to a low value ($H/L < 0.3$). The latter part may therefore belong to S, whereas the early part is designated as C3, despite a correlation between the *L*- and *H*-band fluxes.

3.2. *Correlation of Two Energy Bands*

These features are summarized in Table 2. In each phase, we give the average count rates (*L*, *H*) with statistical errors (δL, δH) and the standard deviations (σ_L, σ_H) which represent variabilities in the respective bands. Comparison of the error and the standard deviation indicates flux variation during the period. The correlation coefficients (*R*) between the *L*- and *H*-band fluxes are shown in the last column.

In Figure 2*a*, the *H*-band flux is plotted against the *L*-band flux during C1 with crosses and during F1 with open circles. In Figure 2*b*, data are plotted during C2 and F2. Data points in each figure are scattered along a constant *H*-band flux of ~ 2 counts s^{-1} and 2.5 counts s^{-1}, respectively. On the other hand, the similar plots for S1 and S2 in Figure 2*c* show a good correlation between two bands, where both bands vary together.

4. SPECTRAL CHANGE

4.1. *Classification of Data*

The X-ray spectra of NGC 4051 in previous observations have been analyzed by data sorting with the total flux (Lawrence et al. 1987; Matsuoka et al. 1990). However, the time behavior differs from energy band to energy band, as shown in the previous section. That section warns that the classification by the total flux alone mixes up data points with different spectral properties. At the same time, such a classification ignores the chronological evolution of spectra. There-

TABLE 2

COUNT RATE IN EACH PHASE

Data Series	Time (s)	L^a (counts s^{-1})	$\sigma_L{}^b$ (counts s^{-1})	δL^c (counts s^{-1})	H^d (counts s^{-1})	$\sigma_H{}^b$ (counts s^{-1})	δH^c (counts s^{-1})	R^e
C1	6912	4.09	1.02	0.35	1.81	0.31	0.30	0.33
F1	3072	7.95	1.26	0.36	2.10	0.29	0.28	0.22
S1	7168	6.06	1.54	0.35	1.70	0.45	0.28	0.80
C2	6400	6.75	0.82	0.40	2.59	0.42	0.33	0.11
F2	1792	10.30	1.33	0.42	2.59	0.28	0.32	0.51
S2	3584	5.71	1.35	0.40	1.50	0.38	0.32	0.51
C3	4352	6.30	2.30	0.46	2.30	0.61	0.33	0.65
S3	8960	5.89	1.67	0.36	1.54	0.43	0.29	0.62
C1 + F1	9984	5.25	2.07	0.35	1.90	0.33	0.29	0.42
C2 + F2	8192	7.53	1.76	0.40	2.59	0.39	0.33	0.10
S1 + S2	10752	5.94	1.47	0.36	1.63	0.44	0.29	0.73

[a] Average count rate in the L band (2.3–6.4 keV).
[b] Standard deviation of the L- (H-) band data points of 256 s.
[c] Statistical error of each L- (H-) band data point of 256 s.
[d] Average count rate in the H band (8.7–20.9 keV).
[e] Correlation coefficient between the H- and L-band fluxes.

fore, we divide all data into eight data series for the spectral analyses, as given in Table 2.

4.2. *Single Power-Law Model*

As the simplest model, the eight spectra were modeled with a single power law with a photon index of Γ, plus the 6.4 keV iron K line (actually 6.385 keV if z is assumed to be 0.0023) intensity I_{Fe} and with the absorption column N_H. The model spectrum is explained as

$$F(E) = (CE^{-\Gamma} + I_{Fe}) \exp [-\sigma(E)N_H] \quad \text{(photons cm}^{-2}\text{ s}^{-1}\text{ keV}^{-1}\text{)} . \quad (1)$$

Figures 3*a* (C1), 3*b* (F1), and 3*c* (S1) are the spectra obtained on the first day with the best-fit single power-law models. The best-fit parameters are summarized in Table 3 with errors for 90% confidence levels. In this process, data below 2.3 keV are neglected, because this energy range is affected by the soft excess component, common in Seyfert I's. Actually, spectra below 3 keV cannot be explained by any combination of absorption column and power index but may require another soft component.

Reduced χ^2 values shown in the last column are acceptable for F1, S1, F2, S2, and S3. The photon index Γ ranges from 1.84 through 2.16, and the neutral hydrogen column density ranges from $10^{21.84}$ through $10^{22.07}$ cm^{-2}, which are consistent with the *EXOSAT* ME data. On the other hand, C1, C2, and C3 show smaller photon indices of 1.59 and 1.70 and exhibit larger reduced χ^2 values (1.346, 1.914, and 1.242, respectively). The residuals of these spectra for a single power-law model result from a hump above 10 keV. A single power-law model, in which the hump is explained by a decrease in photon index, cannot succeed in achieving an acceptable fit for C1, C2, and C3. It implies that some modification of modeling is necessary to describe the spectra above 10 keV of C1 (see residuals from the model shown in the lower panel of Fig. 3*a*).

4.3. *Reflection Model*

Because of poor statistics above 10 keV in previous observations, such a high energy hump had never been recognized, until Matsuoka et al. (1990) and Pounds et al. (1990) found similar features in the spectra of some Seyfert I galaxies with *Ginga*. The existence of this high-energy hump had been theoretically predicted by Lightman & White (1988), Guilbert & Rees (1988), and Ferland & Rees (1988), assuming the reflection component from cold material around or within the non-thermal central energy source of AGNs. The observed spectrum is explained as a combination of the direct and scattered components,

$$F(E) = \{CE^{-\Gamma}[1 + f \times \text{Scat}(E)] + I_{Fe}\} \exp [-\sigma(E)N_H] \quad \text{(photons cm}^{-2}\text{ s}^{-1}\text{ keV}^{-1}\text{)} \quad (2)$$

TABLE 3

SINGLE POWER-LAW FITTING PARAMETERS[a]

Data Series	Normalization Factor (photons s^{-1} keV^{-1})	Index Γ	Fe Line (photons s^{-1})	EW (eV)	N_H (H cm^{-2})	χ^2_ν
C1	12.2 ± 3.0	1.59 ± 0.12	0.114 ± 0.094	182 ± 150	22.20 ± 0.24	1.346
F1	56.3 ± 13.7	2.16 ± 0.13	0.349 ± 0.163	344 ± 161	22.07 ± 0.24	0.901
S1	25.5 ± 4.0	1.85 ± 0.08	0.214 ± 0.086	263 ± 106	21.94 ± 0.24	1.198
C2	22.1 ± 3.8	1.70 ± 0.08	0.171 ± 0.108	182 ± 115	22.01 ± 0.24	1.914
F2	48.4 ± 9.1	1.93 ± 0.10	0.080 ± 0.175	≤ 130	21.84 ± 0.35	0.246
S2	26.8 ± 6.1	1.90 ± 0.12	0.131 ± 0.122	166 ± 155	22.01 ± 0.30	0.931
C3	20.7 ± 2.4	1.70 ± 0.07	0.068 ± 0.123	≤ 139	22.00	1.242
S3	25.0 ± 2.0	1.84 ± 0.05	0.203 ± 0.081	248 ± 99	22.00	0.693

[a] Errors corresponding to 90% confidence level are shown.

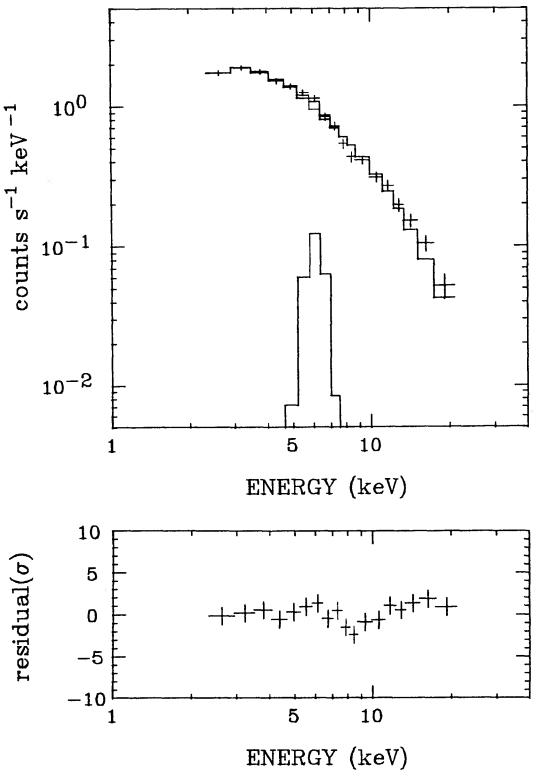

FIG. 3*a*

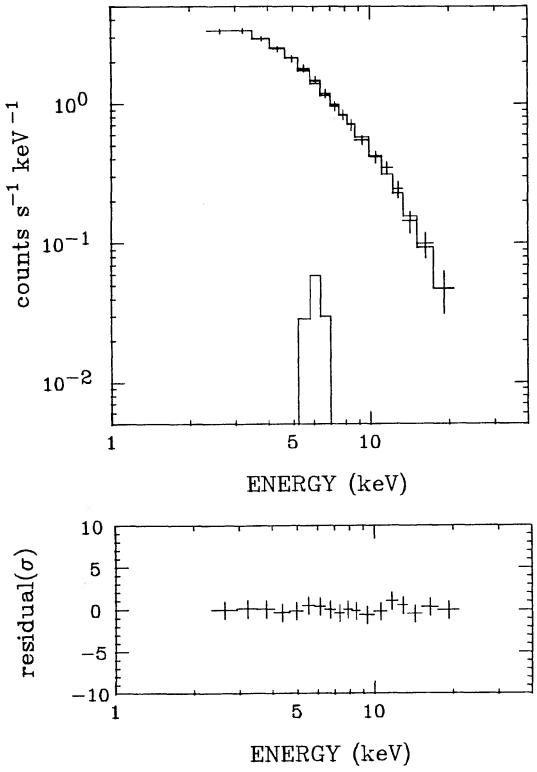

FIG. 3*b*

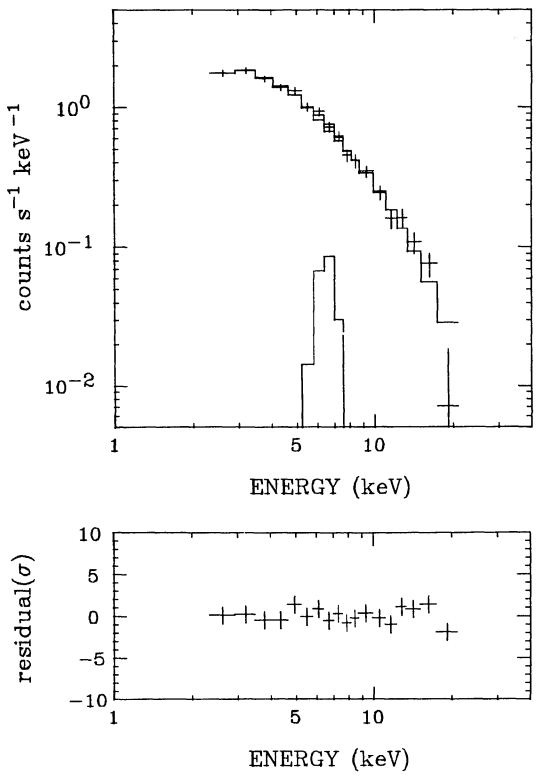

FIG. 3*c*

FIG. 3.—Energy spectra with a single power-law model. (*a*) Energy spectrum in the C1 phase. (*b*) Spectrum in the F1 phase. (*c*) Spectrum in S1 phase. In the lower panel, residuals from the model spectra are presented in units of σ (statistical error). Best-fit parameters are shown in the tables.

where $f(=\Omega/4\pi)$ is the fraction of solid angle covered by the cold matter, and Scat(E)[1] is the energy-dependent reflectivity by a cold slab. Though the iron line flux is included as an independent parameter in equation (2), it should be consistent with the scattered flux or f, because both the iron fluorescence line and the reflected component are to originate from the same reprocessing cold slab. According to a simulation of photon scattering in a cold slab, the covering fraction f of 0.7 yields the iron line equivalent width EW of 120 ~ 150 eV with the photon indices of $\Gamma = 1.6$–2.0, which is consistent with the average iron line equivalent width of about 150 eV observed for NGC 4051.

The results of fitting the observed spectra with the equation (2) are summarized in Table 4, fixing f to be 0.7. Comparing them with those in Table 3, fittings are slightly improved with nearly the same value of parameters. However, the fitting to the C2 spectrum (Fig. 4) is still not acceptable. The unacceptably high value of $f = 2$–3 would be required to explain the high-energy hump. We, therefore, introduce a nonuniform absorption model to explain the spectra in the C phases.

4.4. *Blob Model*

Matter surrounding the central X-ray source may not be uniform but clumpy, as has been indicated by a variety of observations and their interpretations (see, for example, Tsuruta 1988). The clumped matter is represented by blobs, and some of them may partially cover the X-ray source. If a single blob of an optical depth for absorption $\tau(E)$ $[=\sigma(E)N_{\rm blob}]$ covers a fraction p of the source, the X-ray spectrum is modified by a factor $[(1-p)+p\exp(-\tau)]$, as pro-

[1] Scat(E) = $5.39\times10^{-4}\times E^{2.63}$ ($E \le 7.1$ keV)
= $1.0-\exp(-7.26\times10^{-4}\times E^{2.13})$ ($E \ge 7.1$ keV).

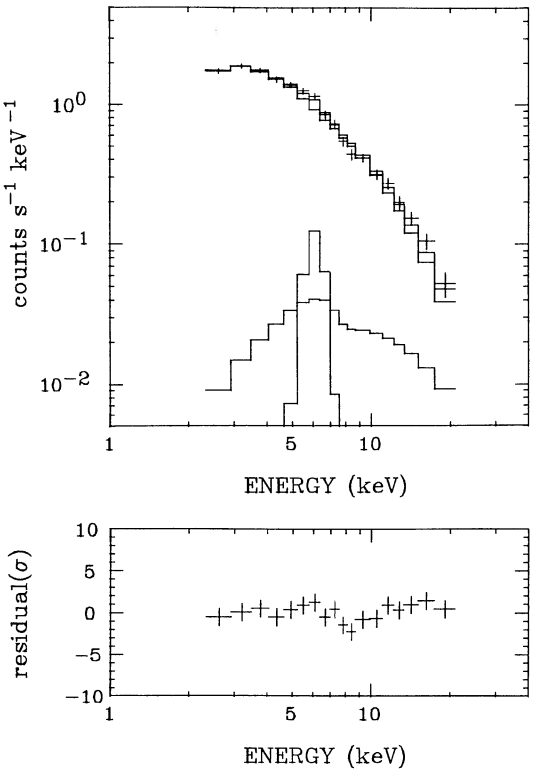

FIG. 4.—Energy spectrum in the C1 phase with a reflection model. Best-fit parameters are listed in Table 4.

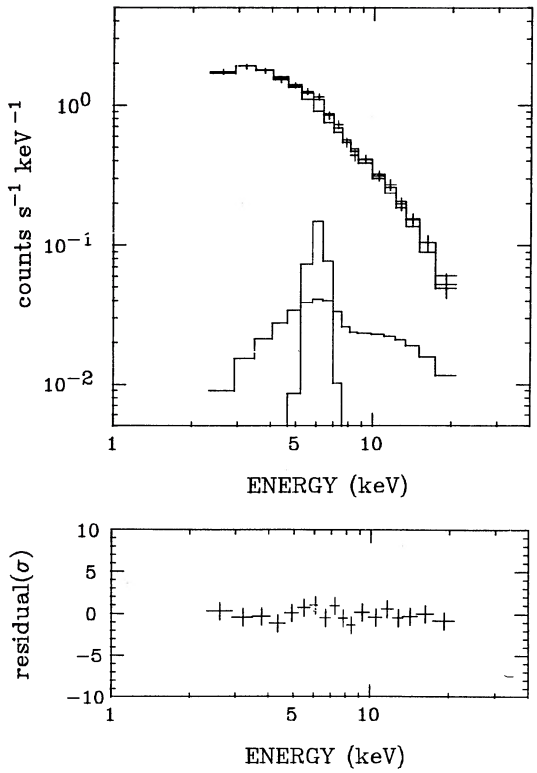

FIG. 5.—Energy spectrum in the C1 phase with a (reflection + blob) model. Best-fit parameters are listed in Table 5.

posed by Watcher, Strauss, & Filippenko (1988) and by Yamauchi (1989) for explaining the observed spectrum. Since $\tau(E)$ decreases rather steeply as energy increases, this modifies the spectrum in such a way that the flux at low energies decreases by a factor $(1 - p)$, while that at high energies is not appreciably modified. If the number of blobs which cover the source is distributed according to the Poisson law, the spectrum (2) is modified to

$$F(E) = \{CE^{-\Gamma}[1 + f \times \mathrm{Scat}(E)] + I_{\mathrm{Fe}}\} \times \exp\{-v[1 - \exp(-\sigma(E)N_{\mathrm{blob}})]\} \times \exp[-\sigma(E)N_{\mathrm{H}}]\ (\mathrm{photons\ cm^{-2}\ s^{-1}\ keV^{-1}}), \quad (3)$$

where v is the average number of blobs on the line of sight, or $[1 - \exp(-v)]$ is the covering factor, $\sigma(E)$ is the absorption cross section, and N_{blob} is the column density of a blob. If $\tau(E) = \sigma(E)N_{\mathrm{blob}} \ll 1$, which holds at high energies, the modification factor is represented by $\exp(-v\tau)$, the same as that for uniform absorption. At low energies, where $\tau(E) \gg 1$, the spectrum is represented by a direct single power-law model reduced by a factor of $\exp(-v)$. If the blob number becomes a fraction of unity, expression (3) can be approximated by $\{(1 - v) + v \exp[-\tau(E)]\}$, which is equivalent to the simple partial covering model.

Fitting the spectra C1, C2, and C3 with equation (3), we obtain acceptable results as shown in Figure 5 and in Table 5. In three C phases, $v \sim 1$ and the hydrogen column density of a blob is (2–3) $\times 10^{24}$ H cm^{-2}. The best-fit values for blob number v close to unity indicate that our blob model is preferred to the partial covering model.

The most important result is that the intrinsic spectrum in the C phase is similar to the F and S phase spectra. In the C

TABLE 4

REFLECTION MODEL FITTING PARAMETERS[a]

Data Series	Normalization Factor (photons s^{-1} keV^{-1})	Index Γ	f_{scat} ($\Omega/4\pi$)	I_{Fe} (photons s^{-1})	N_{H} (H cm^{-2})	χ^2_ν
C1	13.1 ± 1.4	1.65 ± 0.06	0.70	0.113 ± 0.091	22.20	1.055
F1	59.2 ± 5.8	2.21 ± 0.07	0.70	0.346 ± 0.162	22.07	0.857
S1	26.9 ± 1.8	1.91 ± 0.04	0.70	0.214 ± 0.085	21.94	1.049
C2	23.4 ± 1.8	1.75 ± 0.05	0.70	0.170 ± 0.105	22.01	1.500
F2	51.0 ± 4.1	1.98 ± 0.05	0.70	≤ 0.173	21.84	0.226
S2	28.3 ± 2.8	1.95 ± 0.06	0.70	0.131 ± 0.120	22.01	0.875
C3	22.1 ± 2.5	1.76 ± 0.07	0.70	≤ 0.123	22.00	1.015
S3	26.8 ± 2.2	1.91 ± 0.03	0.70	0.203 ± 0.082	22.00	0.678

[a] Errors corresponding to 90% confidence level are shown.

TABLE 5

BLOB AND REFLECTION MODEL FITTING PARAMETERS (FIXED FRACTION OF THE REFLECTION)[a]

Data Series	Normalization Factor (photons s^{-1} keV^{-1})	Index Γ	Fe Line (photons s^{-1})	N_{Hblob} (H cm^{-2})	Blob Number ν	N_H (H cm^{-2})	χ^2_ν
C1	51.1 ± 37.5	1.93 ± 0.26	0.326 ± 0.294	24.37 ± 0.50	0.86 ± 0.54	22.45 ± 0.219	0.708
F1	56.3 ± 13.7	2.16 ± 0.13	0.349 ± 0.163			22.07 ± 0.24	0.901
F1[b]	59.2 ± 5.8	2.21 ± 0.07	0.346 ± 0.162			22.07	0.857
S1[b]	26.9 ± 1.8	1.91 ± 0.04	0.214 ± 0.085			21.94	1.049
C2	79.0 ± 61.4	2.02 ± 0.29	0.437 ± 0.330	24.30 ± 0.46	0.746 ± 0.417	22.32 ± 0.22	1.143
F2	48.4 ± 9.1	1.93 ± 0.10	≤ 0.175			21.84 ± 0.35	0.246
F2[b]	51.0 ± 4.1	1.98 ± 0.05	≤ 0.173			21.84	0.226
S2[b]	28.3 ± 2.8	1.95 ± 0.06	0.131 ± 0.120			22.01	0.875
C3	88.0 ± 68.4	1.98 ± 0.28	≤ 0.316	24.43 ± 0.46	1.03 ± 0.58	22.13 ± 0.22	0.863
S3[b]	26.8 ± 2.2	1.91 ± 0.03	0.203 ± 0.082			22.00	0.678

[a] Errors corresponding to 90% confidence level are shown.
[b] Including reflection component with the angular coverage of $f(=\Omega/4\pi) = 0.7$.

phase, the variation of the L-band flux is due essentially to the modification by blobs, while the H-band flux is not appreciably modifed by the blobs. In the S and F phases, no modification by blobs is required. This implies that blobs disappear from the line of sight in these phases, and the continuum emission region is directly observed. In this model, H-band flux change in the S phase is attributed to an intrinsic luminosity change.

Since the iron line intensity shown in the table is the source flux before being absorbed by the absorption column, the intrinsic line intensity obtained with the blob model should be much higher than that obtained with the single power-law model. The iron line, as well as low energy X-rays, is attenuated by the blobs.

5. DISCUSSION AND CONCLUSIONS

Examining the light curves, we showed that time behaviors in the two energy bands above 8.7 keV and below 6.4 keV are different in the C and F phases. The H-band flux is constant, sometimes over 10,000 s or more, while the L-band flux varies by a factor of 2 on a time scale of 1000 s (doubling time). The constant H-band flux in C1 and F1 is lower than that in C2 and F2. In the S phases, the H- and L-band fluxes change together on a time scale of a few thousands of seconds.

The two types of time behavior thus found can be explained as follows. During the period of C through a soft flare F, the intrinsic X-ray luminosity and spectrum do not appreciably change, but the fraction of soft X-rays absorbed by blobs decreases during the flare. In other words, the X-ray flux above 10 keV, which is free from the modulation by absorption is a good monitor of the intrinsic luminosity. In the S phase, a synchronized change of fluxes in the two energy bands indicates a variation of the intrinsic luminosity with the constant spectrum, which is not appreciably absorbed by blobs.

The fastest doubling (halving) time scale of the L-band X-ray variability δt_L is 1000 s, and that in the H band is $\delta t_H \sim 2000$ s. We have demonstrated that in our natural interpretation the former refers to the variations of the blob numbers in the line of sight, while the latter is due to the intrinsic variability of the X-ray source itself. In general, the source diameter $2R$ has to be smaller than $c \times \delta t$ (c: light velocity, δt: variable time scale). If we use the intrinsic variable time scale $\delta t_H \sim 2000$ s, the source size $2R$ of NGC 4051 has to be smaller than 6×10^{13} cm. It has been pointed out by theoreticians (e.g., Shapiro, Lightman, & Eardley 1976) that the X-rays from a black hole are emitted most effectively at around $5R_S$. Since the Schwarzschild radius R_S is given as $2GM/c^2$, the central mass is estimated to be smaller than $2 \times 10^7 M_\odot$.

The column density of a blob $N_{blob} = 10^{24.3}$ cm^{-2} is required to explain the observed spectra. The blobs responsible for the spectral modulation during the C phase may contribute significantly to the reflection and the fluorescence of the iron K line. However, statistics in the present observation prevent us from drawing a definitive conclusion. A high energy hump in excess of the single power-law (plus blobs for the C phases) spectrum is marginally significant within the attainable statistics, thus favoring the reflection of continuum X-rays by surrounding matter. If the blobs are far from the central X-ray source, little variation would be expected in the associated reflection component. We note that the lack of variation in the deduced intrinsic Fe line flux is consistent with this interpretation.

We thank H. Awaki for much useful discussion, especially on the model calculation of the reflection, and for preparation of software. The contributions by S. T. and K. L. were supported by NASA grants NAG8-782 and NAGW-2208. The data analysis was conducted with a FACOM 380 computer in the High Energy Physics Laboratory of Nagoya University.

REFERENCES

Done, C., Ward, M. J., Fabian, A. C., Kunieda, H., Tsuruta, S., Lawrence, A., Smith, M. G., & Wamsteker, W. 1990, MNRAS, 243, 713
Ferland, G. J., & Rees, M. J. 1988, ApJ, 332, 141
Guilbert, P. W., & Rees, M. J. 1988, MNRAS, 233, 475
Kunieda, H., Turner, T. J., Awaki, H., Koyama, K., Mushotzky, R., & Tsusaka, Y. 1990, Nature, 345, 786
Lawrence, A., Watson, M. G., Pounds, K. A., & Elvis, M. 1985, MNRAS, 217, 685
Lightman, A. P., & White, T. R. 1988, ApJ, 331, 57
Makino, F., et al. 1987, Ap. Letters Comm., 25, 223
Marshall, F. E., Holt, S. S., Mushotzky, R. F., & Becker, R. H. 1983, ApJ, 269, L31

Matsuoka, M., Piro, L., Yamauchi, M., & Murakami, T. 1990, ApJ, 361, 440
Pounds, K. A., et al. 1990, Nature, 344, 132
Shapiro, S. L., Lightman, A. P., & Eardley, D. M. 1976, ApJ, 204, 187
Singh, K. P., Westergaard, N. J., Schnopper, H. W., Awaki, H., & Tawara, Y. 1990, ApJ, 363, 131
Tennant, A. F., Mushotzky, R. F., Boldt, E. A., & Swank, J. H. 1981, ApJ, 251, 464
Tsuruta, S. 1988, in Big Bang, Active Galactic Nuclei, and Supernovae, ed. S. Hayakawa & K. Sato (Tokyo: Universal Academy Press), 293
Turner, M. J. L., et al. 1989, PASJ, 41, 345
Turner, T. J., & Pounds, K. A. 1989, MNRAS, 240, 833
Watcher, K. W., Strauss, M. A., & Filippenko, A. V. 1988, ApJ, 330, 91
Yamauchi, M. 1989, Ph.D. thesis, The Institute of Physical and Chemical Research